6

Soft X-ray and ultra-violet metal-line emission from the gas around galaxies

The gas around galaxies is diffuse and much fainter than the galaxies themselves. A large fraction of the gas has temperatures between $10^{4.5}$ and 10^{7} K. If the gas has metallicities above 0.1 $Z_{\odot}$, it will cool primarily through metal-line emission. With current and upcoming instruments we may be able to detect the halo gas in emission, either directly or statistically. We stack the galaxies in several large cosmological, hydrodynamical simulations and calculate the expected metal-line surface brightness as a function of radius from the centre. We then compare it to the capabilities of current and future facilities. At low redshift, proposed X-ray telescopes can detect O VIII emission out to the virial radius of groups and clusters (assuming a detection limit of 10^{-1} photon s^{-1} cm^{-2} sr^{-1}). C VI, N VII, O VII, and Ne X can also be detected to smaller radii, $0.1 - 0.5R_{vir}$. At high redshift it will be possible to observe rest-frame UV lines, C III, C IV, O VI, Si III, and Si IV, out to $10 - 20$ per cent of the virial radius in haloes larger than 10^{11} $M_{\odot}$ with upcoming instruments (assuming a detection limit of 10^{-20} erg s^{-1} cm^{-2} $arcsec^{-2}$). Most of these lines have surface brightnesses a factor of a few higher at low redshift and could therefore easily be detected with the next generation UV space telescope. The metal-line emission is, in general, biased towards regions of high density and high metallicity and also towards the temperature where the emissivity peaks. This bias varies with radius, halo mass, redshift and between different emission lines. We can quantify the clumpiness of the emitting gas with respect to the underlying density using the clumping factor. The clumping factor is highest in the most massive haloes, because for these haloes the mass-weighted temperature is much higher than the peak emissivity temperature and the emission is thus dominated by cold, dense clumps. The X-ray-flux-weighted properties are similar for all metal lines considered, whereas the UV-flux-weighted properties vary strongly between metal lines.

Freeke van de Voort & Joop Schaye
Monthly Notices of the Royal Astronomical Society
To be submitted

6.1 Introduction

Haloes grow by accreting gas from their surroundings, the intergalactic medium (IGM), which is the main reservoir of baryons. Galaxies grow by accreting gas from their haloes, from which they can form stars. Some of the gas is returned to the circumgalactic medium (CGM) in galactic winds driven by supernovae or active galactic nuclei. Metals produced in stars are also blown out of the galaxy and enrich the CGM. To understand the evolution of galaxies, one needs to study the evolution of the halo gas.

UV and X-ray absorption line studies have revealed cold, neutral gas and the warm-hot intergalactic medium around galaxies. Unfortunately, this type of observation can only provide information along the line of sight, so there is no information about the transverse extent of the absorbing gas cloud. Another limitation is that we can only probe gas in case there is a bright background object. Therefore, absorption line studies are excellent for the regions of moderate overdensity in the IGM, but because galaxies are rare, the statistics are poor for relatively dense halo gas.

The gas emissivity scales with the square of the density. The signal is thus dominated by high-density regions and more sensitive to the CGM than to the general IGM. In this way, emission line studies complement absorption line studies. They have the added advantage of providing a two-dimensional image, in addition to the third dimension provided by the redshift of the emission line, allowing us to study the three-dimensional spatial distribution.

H I Lyman-α (Lyα) emission originates from regions with $T \approx 10^4$ K. It therefore provides an excellent route to studying cold gas in the CGM. Diffuse Lyα emission has been (statistically) detected around high-redshift galaxies at $z \sim 3$ (e.g. Steidel et al., 2000; Matsuda et al., 2004; Bower et al., 2004; Steidel et al., 2011). A large fraction of the halo gas is expected to heat to temperatures above $10^{4.5}$ K, either through photo-ionization, accretion shocks, or through shocks caused by galactic winds. UV metal-line emission enables us to probe gas with $T = 10^{4.5-5.5}$ K, which is more diffuse than colder Lyα emitting gas and a better probe of the average gas properties around galaxies. X-ray metal-line emission traces even hotter gas $T = 10^{6-7}$ K, which is the relevant temperature of the halo gas around high-mass galaxies and in galaxy groups. At $T \sim 10^{4.5-7}$ K the emission is dominated by metal lines for $Z \gtrsim 0.1$ $Z_\odot$ (e.g Wiersma et al., 2009a) and not by hydrogen lines or continuum emission as is the case at lower and higher temperatures.

Dilute halo gas that has been shock-heated to the virial temperature is routinely detected in X-ray observations of the centres of clusters and groups of galaxies, and it may even have been seen around individual galaxies (e.g. Crain et al., 2010a,b; Anderson & Bregman, 2011; Li & Wang, 2012). Most of the detections are made in X-ray continuum emission and Fe lines, see Böhringer & Werner (2010) for a recent review. In the last year, a lot of progress has been made on observing X-ray emission close to the virial radii of clusters (Simionescu

et al., 2011; Akamatsu et al., 2011; Miller et al., 2011; Urban et al., 2011), but see also Eckert et al. (2011). Additionally, there are claims of detections of metal lines (e.g. Kaastra et al., 2003; Takei et al., 2007), whereas other observations set upper limits at lower values than these claimed detections (e.g. Mitsuishi et al., 2011, and references therein).

Observing metal-line emission from diffuse halo gas would yield a lot of information about the physical state of the gas, the distribution of metals, and thus the cycle of gas between haloes and galaxies. In general, however, emission from gas outside of galaxies is faint and thus difficult to detect. Many missions have been proposed to study the diffuse halo gas in emission. With the next generation of spectrographs we should be able to detect certain metal lines. Motivated by future instrumentation and recent proposals, recent studies have quantified the expected emission using cosmological, hydrodynamical simulations (Furlanetto et al., 2004; Bertone et al., 2010a,b; Takei et al., 2011; Frank et al., 2011; Bertone & Schaye, 2012). These studies are focussed mostly on quantifying the emission expected from the warm-hot intergalactic medium in a large section of the Universe or in mock datacubes.

It is possible to increase the signal-to-noise by stacking many observations, centred on a galaxy. In this way we cannot study the halo gas around a single object, but we can characterize the general properties of gas around a certain type of galaxy. In this work we will quantify the expected surface brightness (SB) for the brightest metal lines for a range of halo masses, both in UV at high and low redshift and in soft X-ray at low redshift. Our study complements previous work by predicting mean surface brightness profiles for different halo masses.

In Section 6.2 we describe the simulations we used, how we identify haloes, and how we calculate the emission signal. The results obtained for soft X-ray lines at $z = 0.125$ and UV lines at $z = 0.125$ and $z = 3$ and their detectability are described in Section 6.3. This Section also contains the prediction for H I Balmer-α (Hα). Finally, we conclude in Section 6.4.

In all our calculations we assume the same cosmological parameters as during our simulation (see Section 6.2.1). Most notably $\Omega_\mathrm{m} = 1 - \Omega_\Lambda = 0.238$ and $h = 0.73$.

6.2 Method

6.2.1 Simulations

We use a modified version of GADGET-3 (last described in Springel, 2005b), a smoothed particle hydrodynamics (SPH) code that uses the entropy formulation of SPH (Springel & Hernquist, 2002), which conserves both energy and entropy where appropriate. This work is part of the OverWhelmingly Large Simulations (OWLS) project (Schaye et al., 2010), which consists of a large number of cos-

mological simulations with varying (subgrid) physics. Here we make use of the so-called 'reference' model. The model is fully described in Schaye et al. (2010) and we will only summarize its main properties here.

The simulations assume a ΛCDM cosmology with parameters $\Omega_{\rm m} = 1 - \Omega_\Lambda = 0.238$, $\Omega_{\rm b} = 0.0418$, $h = 0.73$, $\sigma_8 = 0.74$, $n = 0.951$. These values are consistent[1] with the WMAP year 7 data (Komatsu et al., 2011). In the present work, we use the simulation output at redshifts 3 and 0.125.

A cubic volume with periodic boundary conditions is defined, within which the mass is distributed over 512^3 dark matter and as many gas particles. The box size (i.e. the length of a side of the simulation volume) of the simulations used in this work are 25, 50, and 100 h^{-1} comoving Mpc. The (initial) particle masses for baryons and dark matter are $2.1 \times 10^6 (\frac{L_{\rm box}}{25\ h^{-1}{\rm Mpc}})^3$ $\mathrm{M}_\odot$ and $1.0 \times 10^7 (\frac{L_{\rm box}}{25\ h^{-1}{\rm Mpc}})^3$ $\mathrm{M}_\odot$, respectively. The gravitational softening length is $1.95\ (\frac{L_{\rm box}}{25\ h^{-1}{\rm Mpc}})\ h^{-1}$ comoving kpc, i.e. 1/25 of the mean dark matter particle separation, with a maximum of $0.5\ (\frac{L_{\rm box}}{25\ h^{-1}{\rm Mpc}})\ h^{-1}$ proper kpc, which is reached at $z = 2.91$.

Star formation is modelled according to the recipe of Schaye & Dalla Vecchia (2008). A polytropic equation of state $P_{\rm tot} \propto \rho_{\rm gas}^{4/3}$ is imposed for densities exceeding $n_{\rm H} = 0.1$ cm^{-3}, where $P_{\rm tot}$ is the total pressure and $\rho_{\rm gas}$ the density of the gas. Gas particles with proper densities $n_{\rm H} \geq 0.1$ cm^{-3} and temperatures $T \leq 10^5$ K are moved onto this equation of state and can be converted into star particles. The star formation rate (SFR) per unit mass depends on the gas pressure and reproduces the observed Kennicutt-Schmidt law (Kennicutt, 1998) by construction.

Feedback from star formation is implemented using the prescription of Dalla Vecchia & Schaye (2008). About 40 per cent of the energy released by type II supernovae is injected locally in kinetic form, while the rest of the energy is assumed to be lost radiatively. The initial wind velocity is 600 km s^{-1} and the initial mass loading is two, meaning that, on average, a newly formed star particle kicks twice its own mass in neighbouring gas particles.

The abundances of eleven elements released by massive stars and intermediate mass stars are followed as described in Wiersma et al. (2009b). We assume the stellar initial mass function (IMF) of Chabrier (2003), ranging from 0.1 to 100 $\mathrm{M}_\odot$. As described in Wiersma et al. (2009a), radiative cooling and heating are computed element by element in the presence of the cosmic microwave background radiation and the Haardt & Madau (2001) model for the UV/X-ray background from galaxies and quasars assuming the gas to be optically thin and in (photo-)ionization equilibrium.

Using the suite of simulations from OWLS, Wiersma et al. (2011) have shown that galactic winds driven by supernovae are essential for the enrichment of the

[1]The only significant discrepancy is in σ_8, which is 8 per cent, or 2.3σ, lower than the value favoured by the WMAP 7-year data.

IGM. Close to the centre of a halo, most gas has been enriched to $Z > 0.1$ $Z_\odot$, but at the virial radius the scatter is very large (van de Voort & Schaye, 2012).

6.2.2 Identifying haloes

The first step towards finding gravitationally bound structures is to identify dark matter haloes. These can be found using a Friends-of-Friends (FoF) algorithm. If the separation between two dark matter particles is less than 20 per cent of the average separation (the linking length $b = 0.2$), they are placed in the same group. Baryonic particles are linked to a FoF halo if their nearest dark matter neighbour is in that halo. We then use SUBFIND (Dolag et al., 2009) to find the most bound particle of a FoF halo, which serves as the halo centre and also corresponds to the location of the central galaxy. We compute the virial radius, $R_{\rm vir}$, within which the average density agrees with that predicted by the top-hat spherical collapse model in a ΛCDM cosmology (Bryan & Norman, 1998). The halo mass is the mass contained inside $R_{\rm vir}$.

Table 6.1 lists which simulation and halo mass bins are used for various lines and redshifts. It also lists the median halo mass, median stellar mass, median star formation rate, and the number of haloes in the different mass bins.

6.2.3 Emission

We calculate the emissivities of the gas following Bertone et al. (2010a). We only summarize the method here and refer the reader to Bertone et al. (2010a) for details on the procedure. The names and wavelengths of the lines considered in this work are given in Table 6.2 for soft X-rays, which also includes the energy of the lines, and in Table 6.4 for UV and Hα.

We created emissivity tables as a function of temperature, density, and redshift with the photo-ionization package CLOUDY, which was last described in Ferland et al. (1998). The gas is assumed to be optically thin and in ionization equilibrium in the presence of the cosmic microwave background and the Haardt & Madau (2001) UV background. These assumptions were also made when calculating cooling rates during the simulation (Wiersma et al., 2009a) and are thus fully consistent with the simulation. We further assumed solar abundances when creating the tables, but the results are scaled to the abundances derived from the simulation. The tables are created for temperatures 10^2 K$< T < 10^{8.5}$ K with $\Delta{\rm Log}_{10}T = 0.05$ bins and densities 10^{-8} cm^{-3} $< n_{\rm H} <$ 10 cm^{-3} with $\Delta{\rm Log}_{10}n_{\rm H} = 0.2$ bins.

We calculate the emission only for gas with $n_{\rm H} < 0.1$ cm^{-3}, which is therefore not star forming. Our simulations do not resolve the multiphase interstellar medium at $n_{\rm H} \geq 0.1$ cm^{-3}. As we are interested in determining the emission from diffuse gas in haloes, this is consistent with our aims.

The emissivity, ϵ, for an emission line is derived from the tables as a function of ${\rm Log}_{10}T$ and ${\rm Log}_{10}n_{\rm H}$ through interpolation. A gas particle's luminosity is

Table 6.1: List of the simulation box sizes and halo mass ranges used for different emission lines at different redshifts. Included are also the median halo mass, median stellar mass, median star formation rate, and the number of haloes in each halo mass bin.

redshift	band	simulation	$\mathrm{Log}_{10}M_{\mathrm{halo}}$ range	$\mathrm{Log}_{10}M_{\mathrm{halo}}$	$\mathrm{Log}_{10}M_{\mathrm{star}}$	SFR	# haloes
0.125	X-ray	100 h^{-1}Mpc	12-13 [$\mathrm{M}_\odot$]	12.3 [$\mathrm{M}_\odot$]	10.8 [$\mathrm{M}_\odot$]	8.9 $\mathrm{M}_\odot\,\mathrm{yr}^{-1}$	2771
			13-14 [$\mathrm{M}_\odot$]	13.2 [$\mathrm{M}_\odot$]	11.8 [$\mathrm{M}_\odot$]	46 $\mathrm{M}_\odot\,\mathrm{yr}^{-1}$	301
			14-15 [$\mathrm{M}_\odot$]	14.2 [$\mathrm{M}_\odot$]	12.6 [$\mathrm{M}_\odot$]	144 $\mathrm{M}_\odot\,\mathrm{yr}^{-1}$	18
0.125	UV & Hα	50 h^{-1}Mpc	11-12 [$\mathrm{M}_\odot$]	11.3 [$\mathrm{M}_\odot$]	9.3 [$\mathrm{M}_\odot$]	0.05 $\mathrm{M}_\odot\,\mathrm{yr}^{-1}$	2723
			12-13 [$\mathrm{M}_\odot$]	12.3 [$\mathrm{M}_\odot$]	10.9 [$\mathrm{M}_\odot$]	9.3 $\mathrm{M}_\odot\,\mathrm{yr}^{-1}$	374
			13-14 [$\mathrm{M}_\odot$]	13.2 [$\mathrm{M}_\odot$]	11.7 [$\mathrm{M}_\odot$]	39 $\mathrm{M}_\odot\,\mathrm{yr}^{-1}$	46
3.0	UV	25 h^{-1}Mpc	10-11 [$\mathrm{M}_\odot$]	10.3 [$\mathrm{M}_\odot$]	8.2 [$\mathrm{M}_\odot$]	0.11 $\mathrm{M}_\odot\,\mathrm{yr}^{-1}$	1857
			11-12 [$\mathrm{M}_\odot$]	11.3 [$\mathrm{M}_\odot$]	9.5 [$\mathrm{M}_\odot$]	4.2 $\mathrm{M}_\odot\mathrm{yr}^{-1}$	117
			12-13 [$\mathrm{M}_\odot$]	12.2 [$\mathrm{M}_\odot$]	11.0 [$\mathrm{M}_\odot$]	111 $\mathrm{M}_\odot\,\mathrm{yr}^{-1}$	5

then

$$L = \epsilon(z, T, n_{\rm H}) \frac{m_{\rm gas}}{\rho} \frac{X_y}{X_y^{\odot}} \tag{6.1}$$

in erg s^{-1}, where $m_{\rm gas}$ is its mass, ρ is its density, X_y is the 'SPH-smoothed' mass fraction of the element corresponding to the emission line, and $X_y^{\odot}$ is the solar mass fraction of the same element. We use smoothed abundances as described by Wiersma et al. (2009b). This is consistent with the simulation, because these smoothed abundances were also used in the simulation to compute the cooling rates. The flux is

$$F = \frac{L}{4\pi d_{\rm L}^2} \tag{6.2}$$

in erg s^{-1} cm^{-2}, or

$$F = \frac{L}{4\pi d_{\rm L}^2} \frac{\lambda}{h_{\rm p} c} (1+z) \tag{6.3}$$

in photon s^{-1} cm^{-2}, with $d_{\rm L}$ the luminosity distance, $h_{\rm p}$ the Planck constant, c the speed of light, and λ the rest-frame wavelength of the emission line.

To calculate the emission profiles, we project the flux using a flux-conserving SPH interpolation scheme onto a two-dimensional grid, centred on the halo centre. The surface brightness is calculated by dividing the flux by the solid angle subtended by a pixel either in arcsec^2 or in sr,

$$S_{\rm B} = F/\Omega. \tag{6.4}$$

In this paper, we investigate the detectability of the emission lines listed in Tables 6.2 and 6.4, originating from circumgalactic gas. We quantify the expected surface brightness as a function of radius for a range of halo masses. Our predictions made should be considered with care. We did not take into account the velocities of the gas and thus the width of the lines, nor the effect of the atmosphere. A robust study of detectability should produce datacubes, including noise, and analyze them using the same pipeline as the observations. This is beyond the scope of the present work in which we show and discuss the theoretically expected surface brightnesses.

O VII is a line triplet at 0.574, 0.568, and 0.561 keV. The first line is a resonance line, the second one an intercombination line and the last one a forbidden line. Resonance photons have large cross-sections and will be scattered in random directions, giving rise to lower observed fluxes or even absorption. The intercombination line is significantly weaker ($0.5 - 0.6$ dex) than the other two. The resonance line is only slightly stronger than the forbidden line (by about 0.1 dex) without taking into account attenuation. The actual 0.574 keV surface brightness may be much lower due to resonant scattering. We therefore only show the surface brightness of the forbidden line at 0.561 keV, but note that if the emission at all three wavelengths is added together, the signal could be more than twice as strong.

Table 6.2: List of ion, rest-frame wavelength, and energy for the X-ray emission lines used in this work.

ion	λ (Å)	E (keV)
C VI	33.74	0.367
N VII	24.78	0.500
O VII	22.10	0.561
O VIII	18.97	0.654
Ne X	12.14	1.021

The UV doublets, C IV, O VI, and Si IV, have flux ratios of 2:1. We consider only the strongest line in this paper, but the results for the weaker lines thus follow directly.

6.3 Results

6.3.1 Soft X-ray

Current X-ray telescopes, i.e. *Chandra* and *XMM-Newton*, have not detected metal-line emission from diffuse, intergalactic gas, which is consistent with the predictions (Yoshikawa et al., 2003, 2004; Fang et al., 2005). To map the halo gas with future instruments, a combination of high angular and spectral resolution and a large field of view are preferred (Bertone et al., 2010a). As the emission is dominated by bright, compact regions, high angular resolution is necessary prevent smearing out the emission, in which case it would be harder to detect as well as impossible to correctly identify its origin. *ASTRO-H*[2] will be launched in a few years, but its field of view is rather small and its spatial resolution is coarse (e.g. Soong et al., 2011). Therefore, it is not an ideal instrument for studying halo X-ray profiles. A number of X-ray missions have been proposed in the past years, such as *IXO/ATHENA*[3] and *ORIGIN* (den Herder et al., 2011). Their proposed specifications are listed in Table 6.3, as are those for existing and future UV instruments, which are discussed in Sections 6.3.2 and 6.3.3.

The instrumental background is 2×10^{-2} photon $s^{-1}cm^{-2}keV^{-1}$, which corresponds to 1.3×10^{3} photon $s^{-1}sr^{-1}keV^{-1}$ for CRIS on *ORIGIN* (with a pixel size of 300 μm and 24 arcsec). In the narrow field mode, the energy resolution is 2.5 eV, so this corresponds to 3 photon $s^{-1}sr^{-1}$. For an effective area of 10^{3} cm^{2}, the surface brightness of the instrumental background equals 3×10^{-3} photon $s^{-1}cm^{-2}sr^{-1}$. (It would be twice as much in the wide field mode.)

For XMS on *IXO/ATHENA* the instrumental background is also 2×10^{-2} photon $s^{-1}cm^{-2}keV^{-1}$, which corresponds to 8.5×10^{4} photon $s^{-1}sr^{-1}keV^{-1}$ (with

[2]http://astro-h.isas.jaxa.jp/
[3]http://ixo.gsfc.nasa.gov/, http://sci.esa.int/ixo

Table 6.3: Summary of technical specifications for instruments discussed in the main text.

Telescope (instrument)	Field of view (arcmin^2)	Angular resolution (arcsec)	Spectral resolution
ORIGIN (CRIS)	10×10 (30×30)	30	2.5 (5) eV
IXO/ATHENA (XMS)	2×2 (5×5)	5	2.5 (10) eV
ASTRO-H (SXS)	3×3	78	5 eV
FIREBALL	2.67×2.67	10	0.4 Å
Hale (CWI)	1×0.67	2.5×1	0.12 Å
Keck (KCWI)	$0.33 \times (0.14 - 0.57)$	$0.35 - 1.4$	0.03-0.6 Å
VLT (MUSE)	1×1	0.2	0.4 Å

a pixel size of 300 μm and 3 arcsec). For an energy resolution of 2.5 eV, which is appropriate for the narrow field mode, this corresponds to 2×10^2 photon $s^{-1}sr^{-1}$. For an effective area of 3×10^4 cm^2, the surface brightness of the instrumental background equals 7×10^{-3} photon $s^{-1}cm^{-2}sr^{-1}$. (It would be four times as much in the wide field mode.)

Hickox & Markevitch (2006) determined that the unresolved cosmic X-ray background is about 14 ± 1 photon $s^{-1}cm^{-2}sr^{-1}keV^{-1}$ in the energy range we are interested in ($0.5 - 1$ keV). This unresolved signal is dominated by diffuse Galactic emission and local thermal-like emission. Part of this unresolved background could be resolved in deeper observations (Hickox & Markevitch, 2007). We will use the limit of 14 ± 1 photon $s^{-1}cm^{-2}sr^{-1}keV^{-1}$ as it is an upper limit on the unresolved background for future observations. For the energy resolution of CRIS on *ORIGIN* and XMS on *IXO/ATHENA* (i.e. 2.5 eV) this corresponds to about 3×10^{-2} photon $s^{-1}cm^{-2}sr^{-1}$. The instrumental background is therefore lower than the unresolved X-ray background. Observations should be able to probe down to 10^{-1} photon $s^{-1}cm^{-2}sr^{-1}$ without being strongly affected by the background. For this surface brightness a 1 Msec exposure would result in about 2 detected photons per resolution element for a 1 $arcmin^2$ feature with *ORIGIN* at 30 arcsec resolution and *IXO/ATHENA* at 5 arcsec resolution.

Figure 6.1 shows images of the mean surface brightness in the O VIII (0.654 keV) line at $z = 0.125$, which is the brightest soft X-ray line we consider. We use three halo mass bins, corresponding to (the haloes of) galaxies, groups, and clusters, with masses of $M_{\rm halo} = 10^{12-13}$ $M_\odot$, 10^{13-14} $M_\odot$, and 10^{14-15} $M_\odot$ with $R_{\rm vir} \approx 0.25$, 0.51, and 1.1 h^{-1} comoving Mpc, respectively. The images are 3 h^{-1} comoving Mpc on a side, which corresponds to 28 arcmin at $z = 0.125$, and the white circles indicate the median virial radii of the haloes. Haloes with $M_{\rm halo} > 10^{13}$ $M_\odot$ have O VIII emission that is stronger than 10^{-1} photon $s^{-1}cm^{-2}sr^{-1}$ out to $0.7R_{\rm vir}$, whereas for $M_{\rm halo} = 10^{12-13}$ $M_\odot$ this is only the case at $R \lesssim 0.4R_{\rm vir}$.

To make emission profiles for all the metal lines listed in Table 6.2, we calculate the average of the surface brightness azimuthally. In Figure 6.2 we show the mean (median) X-ray line surface brightness profiles for haloes at $z = 0.125$ as solid (dotted) curves. We show the same three halo mass bins as in Figure 6.1 out to twice the median virial radius.

The strongest observable soft X-ray line is O VIII (0.654 keV). It is followed by C VI (0.367 keV) and OVII (0.561 keV) for galaxies. In groups, Ne X (1.021 keV) is the second strongest line in the centre of the halo, but it is much weaker than C VI and O VII in the halo outskirts. As mentioned in Section 6.2.3, O VII is a triplet and the emission will be stronger when adding the contributions of the three lines. For both galaxies and groups, the Ne X profile is steeper than that of all the other lines shown. In clusters C VI and Ne X are of comperable brightness at all radii and about 0.6 dex below O VIII. N VII (0.500 keV) is similar to O VII at all radii for cluster haloes and about an order of magnitude fainter than O VIII. Ne X has the lowest surface brightness for $M_{\rm halo} = 10^{12-13}$ $M_\odot$, but it is as strong as C VI for clusters. We also computed the emissivities of C V (0.308 keV), N VI

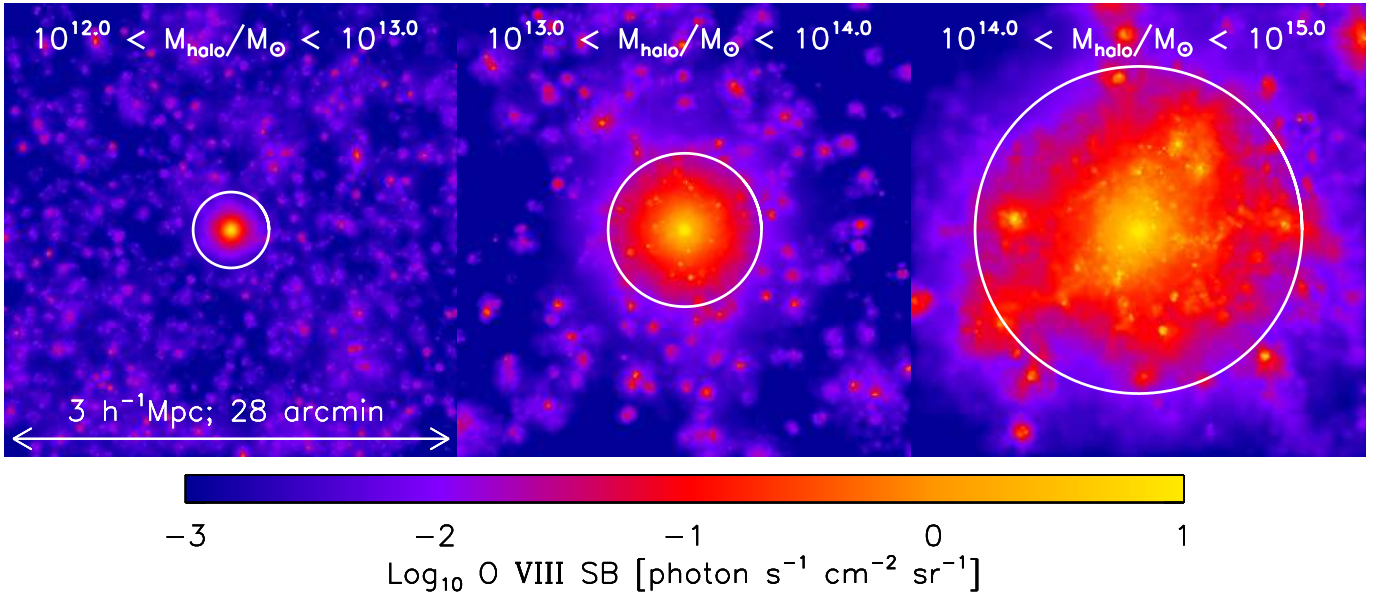

Figure 6.1: Mean O VIII emission maps for haloes with $M_{\rm halo} = 10^{12-13}$ $M_\odot$, 10^{13-14} $M_\odot$, and 10^{14-15} $M_\odot$, from left to right, at $z = 0.125$. The images are 3 h^{-1} comoving Mpc on a side, span 28 arcmin on the sky, and have a pixel size of 5 arcsec. The white circles indicate the median virial radius.

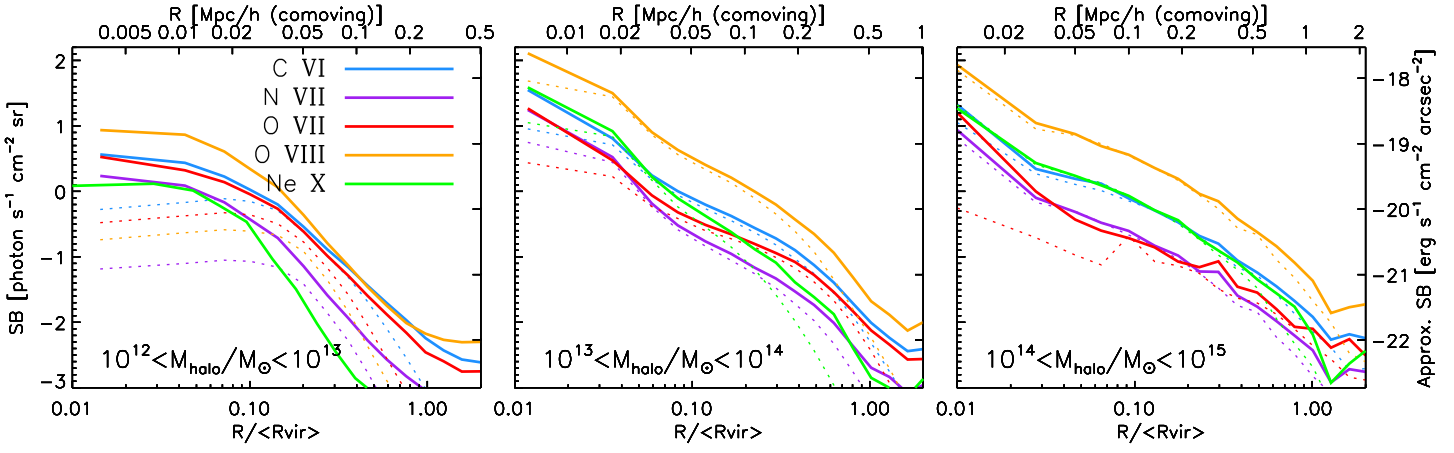

Figure 6.2: Mean surface brightness (solid curves) as a function of radius at $z = 0.125$ for the same haloes as in Figure 6.1 for the X-ray lines indicated in the legend. Dotted curves the median profile. The radius is normalized by dividing by the median virial radius in each mass bin. The surface brightness in photon $s^{-1}cm^{-2}sr^{-1}$ indicated by the left y-axis is exact. For the right y-axis it has been converted to erg $s^{-1}cm^{-2}arcsec^{-2}$ using $\langle\lambda\rangle = 22.2$ Åfor the right axis. The pixel size was 5 arcsec before binning it and the thickness of the region is 5 h^{-1} comoving Mpc. O VIII is the brightest line at all halo masses, followed by C VI. The relative strengths of the lines vary with halo mass. For galaxy-sized haloes, the profiles flatten at $R \lesssim 10\ h^{-1}$kpc, because this region is dominated by the ISM, which we excluded from our analysis.

(0.420 keV), Ne IX (0.922 keV), Mg XII (1.472 keV), Si XIII (1.865 keV), Si XV (2.460 keV), Fe XVII (0.727 keV), which were generally all weaker than the lines shown (see also Bertone et al., 2010a). The emissivities of Ne IX and Fe XVII are as high as those of N X in galaxies and Fe XVII is as high as O VII for $R < 0.2\mathrm{R_{vir}}$ in groups. Both lines are fainter in cluster centres, but possibly still detectable.

At a limiting surface brightness of 10^{-1} photon $\mathrm{s^{-1}cm^{-2}sr^{-1}}$, we would be able to detect O VIII emission out to the 80 per cent of the virial radius of cluster with $M_{\mathrm{halo}} = 10^{14-15}\ \mathrm{M_\odot}$, C VI out to 40 per cent, and O VII and N VII out to 20 per cent. For lower-mass haloes, $M_{\mathrm{halo}} = 10^{13-14}\ \mathrm{M_\odot}$, O VII can be observed out to the same physical scale, 200 h^{-1} comoving kpc, which corresponds to a larger fraction of the virial radius, $0.4R_{\mathrm{vir}}$. In this case, O VIII is observable out to $0.7R_{\mathrm{vir}}$ and C VI out to $0.5R_{\mathrm{vir}}$. For $M_{\mathrm{halo}} = 10^{12-13}\ \mathrm{M_\odot}$, O VIII, O VII, and C VI can be observed out to the same radius of $0.3R_{\mathrm{vir}}$.

The instrumental background for SXS on *ASTRO-H* is even lower, but its angular resolution is much worse and the effective area is very small. It should be able to detect O VIII emission in the centres of groups, but it will not be able to see detailed structure, because the emission would be contained in a single pixel.

Figure 6.3 shows the X-ray flux-weighted median overdensity, clumping factor, temperature, and metallicity. The solid lines and crosses show the result for the gas at $0.1\mathrm{R_{vir}} - 0.5\mathrm{R_{vir}}$, while the dashed lines and triangles show $0.5\mathrm{R_{vir}} - \mathrm{R_{vir}}$. The flux-weighted overdensities of the gas responsible for the different lines are very similar and close to the 84th percentile of the mass-weighted overdensity and this is $\sim 0.2 - 0.7$ dex above the median density. The reason for this is that the emissivity scales as ρ^2, which biases the emission towards high densities. The flux-weighted densities increase by $\sim 0.7 - 0.9$ dex over two orders of magnitude in halo mass, but the mass-weighted median density increases by only 0.4 dex over the same range of halo masses, indicating that the clumpiness of the gas probed by the lines increases with halo mass.

Because the line flux scales with ρ^2 and the mass with ρ, we can quantify the clumpiness of the emitting gas with respect to the underlying density using the clumping factor. In this case the clumping factor is calculated as

$$C = \left(\langle\rho\rangle_{\mathrm{Flux}} / \langle\rho\rangle_{\mathrm{Mass}}\right)^2 \tag{6.5}$$

where $\langle\rho\rangle_{\mathrm{Flux}}$ is the flux-weighted density and $\langle\rho\rangle_{\mathrm{Mass}}$ the mass-weighted density. If the clumping factor is known, it is possible to derive the underlying density profile from metal-line observations. The assumption $C = 1$ is clearly not applicable.

For galaxies and groups, $C \lesssim 3$ and it is lower in the halo outskirts than in the halo core. For clusters, the story is very different. The clumping factor is around 10, with a spread of 0.4 dex for the different lines, so in this case the emission gives a more biased view. The clumping factor is higher in the cluster outskirts than in the centre, possibly indicating that a larger part of the emission originates from satellites.

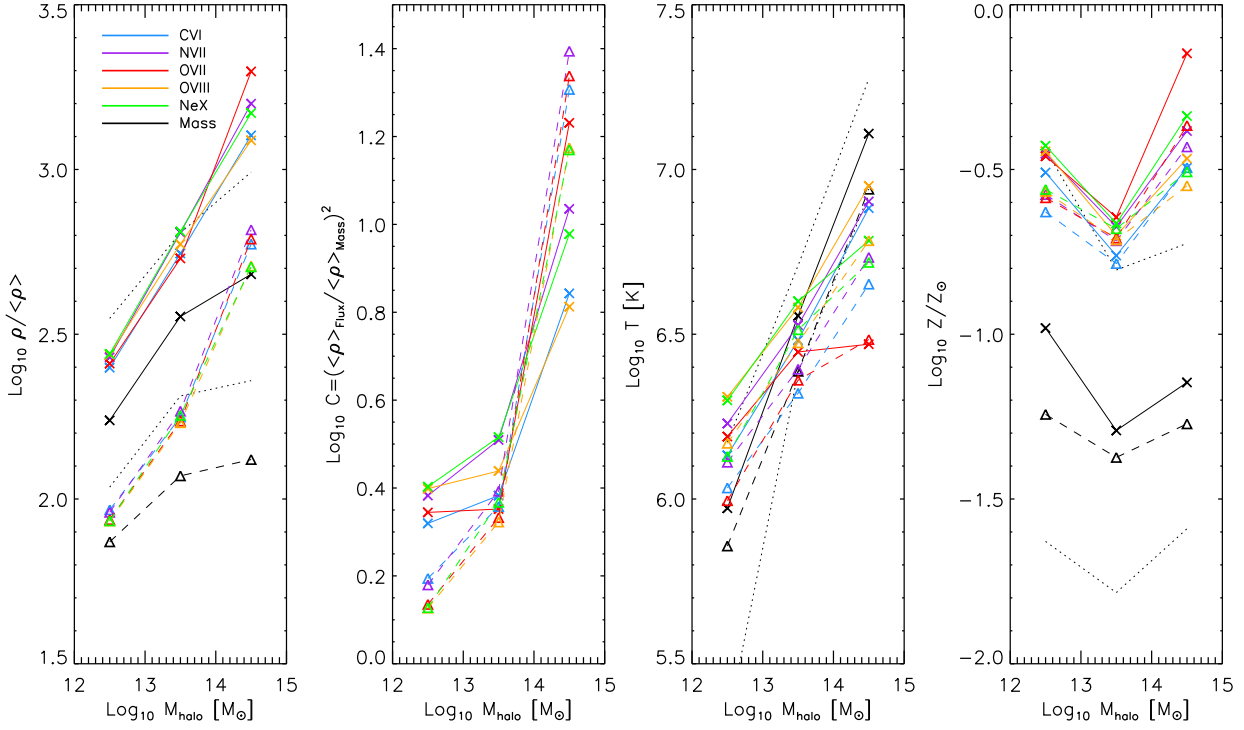

Figure 6.3: Mass-weighted (black curves) and X-ray flux-weighted (colours for different lines as in Figure 6.2) median overdensity, clumping factor, temperature, and metallicity at $z = 0.125$ averaged over haloes with $M_{\rm halo} = 10^{12-13}$ $M_\odot$, $M_{\rm halo} = 10^{13-14}$ $M_\odot$, and $M_{\rm halo} = 10^{14-15}$ $M_\odot$, from left to right. The solid curves and crosses show the result for the gas at $0.1R_{\rm vir} - 0.5R_{\rm vir}$, while the dashed curves and triangles show $0.5R_{\rm vir} - R_{\rm vir}$. The dotted, black curves show the mass-weighted 16th and 84th percentiles for the inner halo. The flux-weighted properties are biased towards high density and metallicity. The flux-weighted temperature is biased towards the temperature at which the line reaches its peak emissivity. The clumping factor is large in clusters.

Table 6.4: List of ion and rest-frame wavelengths for the Hα and UV metal-line emission lines used in this work.

ion	λ (Å)	λ_2 (Å)
H I (Hα)	6563	-
C III	977	-
C IV	1548	1551
O VI	1032	1038
Si III	1207	-
Si IV	1394	1403

The temperature at which the emissivity peaks is highest for Ne X, at $\sim 10^{6.8}$ K, and O VIII, around $10^{6.5}$ K, and it decreases slowly towards higher temperatures (Bertone et al., 2010a). This is the reason why, for galaxies and groups, these lines have the highest flux-weighted temperatures. For clusters, the Ne X-weighted temperature is lower than that of O VIII. The flux-weighted median temperatures increase less steeply with halo mass than the mass-weighted median temperature, although the former still increase by ~ 0.7 dex for an increase of 2 dex in halo mass. For the lowest (highest) mass bin the flux-weighted temperatures are higher (lower) than the mass-weighted temperature. The O VII flux-weighted temperature stays roughly constant with halo mass. This is due to the fact that the emissivity curve of O VII is more strongly peaked in temperature than the emissivity of the other lines (see Figure 1 of Bertone et al., 2010a). It peaks at $10^{6.3}$ K and drops quickly for higher and lower temperatures.

In the halo outskirts, the temperatures probed are somewhat lower, by $0.2 - 0.3$ dex, than in the inner parts. The densities are lower by $0.5 - 0.7$ dex. This is true for flux-weighted as well as mass-weighted median temperatures and densities, so they follow the same trend.

The median mass-weighted metallicity is 0.04-0.1$Z_\odot$, but the flux-weighted metallicities are 0.5-1.0 dex higher. The median flux-weighted metallicities are similar to the 84th percentile of the mass-weighted metallicity, for galaxies and groups. The flux-weighted metallicities for clusters are significantly above the 84th percentile, especially for O VII, which also has the highest overdensity and lowest temperature. Thus, perhaps not surprisingly, X-ray metal-line emission is biased towards high-metallicity gas. As metal lines dominate the emission in the soft X-ray band (0.5-1.0 keV), the same will be true for broad band emission (e.g. Crain et al., 2010a).

6.3.2 Low-redshift UV

For detecting UV metal-line emission as a tracer of halo gas, instruments should ideally have a large field of view and a high spatial and angular resolution, as is also the case for X-ray emission. The emission will be dominated by relatively

high-density material. With high spatial resolution, it will be possible to verify its clumpiness.

A surface brightness limit of order 10^{-18} erg s^{-1}cm^{-2}arcsec^{-2}, as is the case for the *FIREBALL*[4] balloon experiment (Tuttle et al., 2008, 2010), will only be sufficient to detect metal-line emission in the centres of massive haloes. The wavelength range of *FIREBALL* (2000–2200 Å) is such that it will only probe the UV metal lines at a somehat higher redshift than shown here ($z \approx 0.35$ for C IV) where the surface brightness is a bit lower. A detection limit of order 10^{-21} erg s^{-1}cm^{-2}arcsec^{-2} is envisioned for the next generation UV mission *ATLAST* (Postman, 2009).

Figure 6.4 shows images of C III (977 Å) line emission at $z = 0.125$. We use three halo mass bins of $M_{\rm halo} = 10^{11-12}$ M$_\odot$, 10^{12-13} M$_\odot$, and 10^{13-14} M$_\odot$ with $R_{\rm vir} \approx 0.11$, 0.25, and 0.50 h^{-1}Mpc, respectively. The images are 1 h^{-1} comoving Mpc on a side, which corresponds to 9 arcmin at $z = 0.125$. The surface brightness in the haloes with mass below 10^{13} M$_\odot$ looks relatively smooth, because it has been averaged over many haloes (see Table 6.1 . There are only 46 haloes in the last bin and the image looks very patchy. We will discuss the clumpiness of the gas responsible for the emission below.

As in the previous section, we calculate the average of the surface brightness azimuthally for the UV metal lines listed in Table 6.4. We include also Hα from the same haloes and discuss it in Section 6.3.4. Figure 6.5 shows the mean (median) surface brightness profiles for different UV lines for stacked haloes at $z = 0.125$ as the solid (dotted) curves. We use the same three halo mass bins as in Figure 6.4.

C III (977 Å) is the brightest line, followed by Si III (1207 Å). The emission profile for all lines peaks in the halo core, where it may, however, be outshone by the galaxy. O VI (1032 Å) gives the most extended profile, in the sense that the ratio between emission in the halo core and outskirts is largest. This is caused by the fact that O VI traces warmer and more diffuse gas than the other lines. C IV (1548 Å) and Si IV (1294 Å) are weaker than C III and Si III, but because they have frequencies redward of Lyα, they are less easily absorbed. We also computed the emissivities of He II (1640 Å) and N V (1239 Å), which were weaker and therefore not shown.

A surface brightness limit of 10^{-18} erg s^{-1}cm^{-2}arcsec^{-2} should enable us to observe metal-line emission from the centres of fairly massive galaxies ($M_{\rm halo} > 10^{12}$ M$_\odot$. However, it is possible that the galaxy will outshine the halo in these regions.

By stacking haloes, *FIREBALL* could in principle probe down to a surface brightness limit of 10^{-19} erg s^{-1}cm^{-2}arcsec^{-2}. Its wavelenth rage is such that it can only detect C III and Si III at $z \approx 1$. As the surface brightness is lower at $z = 1$ as compared to $z = 0.125$ by ~ 0.5 (not shown), it may see emission out to ~ 0.1R$_{\rm vir}$ for $M_{\rm halo} > 10^{12}$ M$_\odot$. A complicating factor is that C III and Si III have

[4]http://www.srl.caltech.edu/sal/fireball.html

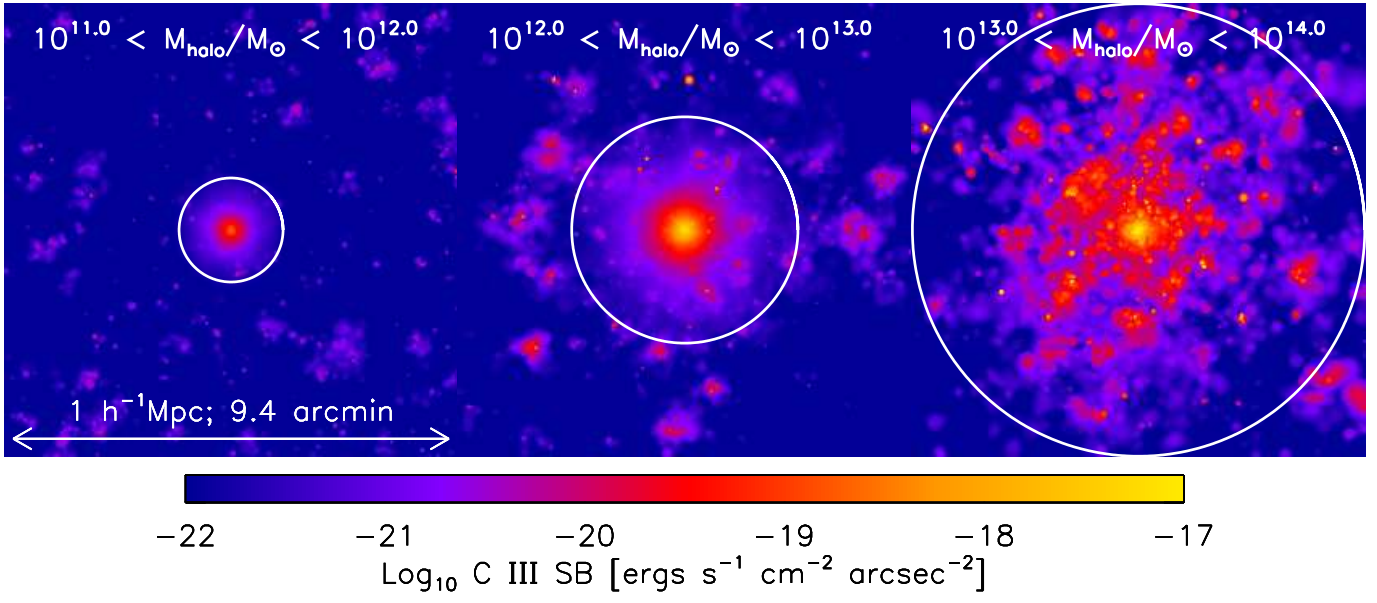

Figure 6.4: Mean C III emission maps for haloes with $M_{\rm halo} = 10^{11-12}$ $M_\odot$, $M_{\rm halo} = 10^{12-13}$ $M_\odot$, and $M_{\rm halo} = 10^{13-14}$ $M_\odot$, from left to right, at $z = 0.125$. The images are 1 h^{-1} comoving Mpc on a side, span 9.4 arcmin on the sky, and have a pixel size of 2 arcsec. The white circles indicate the median virial radius.

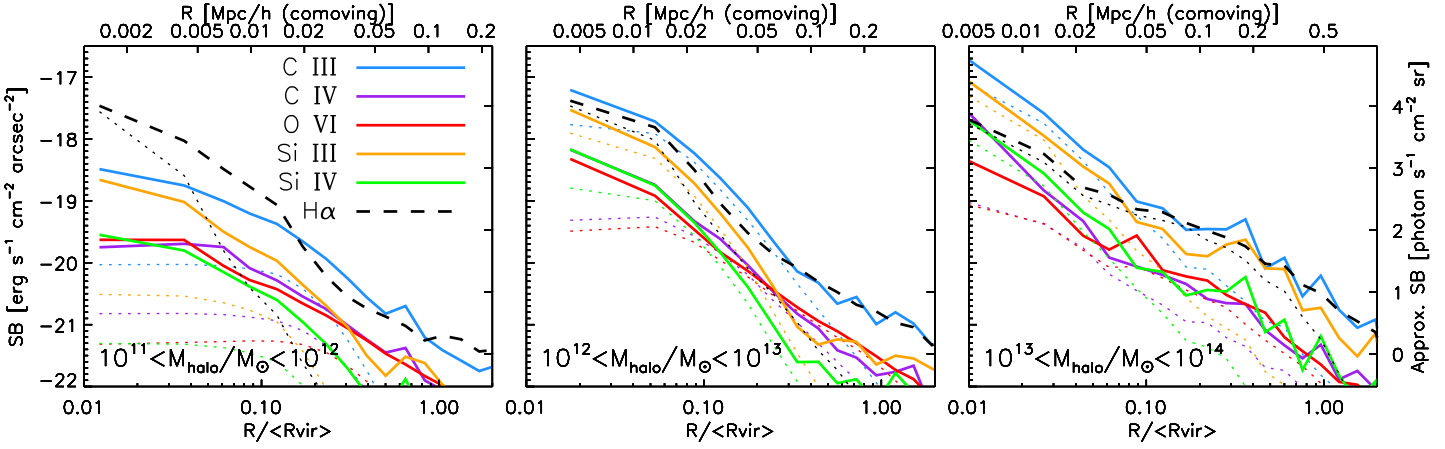

Figure 6.5: Mean UV (solid curves) and Hα (dashed curve) surface brightness as a function of radius at $z = 0.125$ for the same haloes as in Figure 6.4. The emission lines are indicated in the legend. Dotted curves show the median profile. The radius is normalized by dividing by the median virial radius in each mass bin. The surface brightness in erg s^{-1}cm^{-2}arcsec^{-2} on the left y-axis is exact. It has been converted to photon s^{-1}cm^{-2}sr^{-1} using $\langle\lambda\rangle = 1232$ Å. The pixel size was 2 arcsec before it was binned and the thickness of the region is 2.2 h^{-1} comoving Mpc. C III is the brightest line, followed by Si III.

frequencies blueward of Lyα and could therefore be absorbed by intervening hydrogen, an effect that is much worse for C III than Si III.

With a detection limit of order 10^{-21} erg s^{-1}cm^{-2}arcsec^{-2} we would be able to detect C III out to the virial radius and several other metal lines out to 50 per cent of R_{vir}. Such a low surface brightness limit may be attainable for the next generation UV mission *ATLAST* (Postman, 2009). As Lyα emission is even brighter (e.g. Furlanetto et al., 2003), one can even probe the gas in emission outside galactic haloes, in the filaments of the cosmic web.

In Figure 6.6 the UV flux-weighted overdensity, clumping factor, temperature, and metallicity are shown for several metal lines at $z = 0.125$ for the same three halo mass bins as in Figure 6.4. The solid lines and crosses show the result for the gas at $0.1R_{vir} - 0.5R_{vir}$, while the dashed lines and triangles show $0.5R_{vir} - R_{vir}$. The different metal lines probe very different densities, all higher than the mass-weighted overdensity. O VI results in the lowest flux-weighted overdensity. The flux-weighted density increases via C IV to C III to Si IV and is the highest for Si III. For all halo masses, the silicon lines have higher flux-weighted densities than the 84th percentile of the mass-weighted density. In group-sized haloes all lines are dominated by gas denser than the mass-weighted 84th percentile. The difference between the O VI and Si III flux-weighted overdensities is ~ 1 dex. The flux-weighted overdensities increase somewhat more steeply with halo mass than the mass-weighted overdensity, by about 1.5 dex for an increase of 2 dex in halo mass.

Because the median flux-weighted densities vary a lot between different UV metal-lines, the clumping factor, defined in Equation 6.5, does so as well. The clumpiness is lowest for O VI emission and highest for Si III, with a difference in clumping factor of around 1.5 dex for a fixed halo mass. The clumping difference between centre and outskirts is relatively minor, $\Delta Log_{10}C \lesssim 0.2$ dex. For O VI in galaxy haloes ($M_{\rm halo} < 10^{13}$ M$_\odot$), the clumping factor is close to one and hence a good tracer of the density (although it is still biased towards high metallicities). For the metal lines and halo mass range probed, the clumping factor varies between $\sim 1 - 10^3$. This means that the UV metal-line emission is quite clumpy. This is in agreement with Bertone et al. (2010b) and Frank et al. (2011) who find that most of the UV flux comes from discrete, compact sources.

The flux-weighted temperature depends on the specific metal line, decreasing as the corresponding overdensity increases. They are insensitive to the mass-weighted temperature of the halo, because the emissivities are strongly peaked at specific temperatures (Bertone et al., 2010b). The difference between Si III and O VI is just over an order of magnitude. All UV metal-lines probe gas with temperatures $10^{4.5-5}$ K with the exception of O VI, which is dominated by $10^{5.5}$ K gas.

The mass-weighted temperature is up to 0.2 dex lower in the outskirts of the halo than in to the core, but the flux-weighted temperatures differ by at most 0.1 dex. The overdensity is consistently lower by $0.3 - 0.6$ dex in the halo outskirts for both flux-weighted and mass-weighted densities.

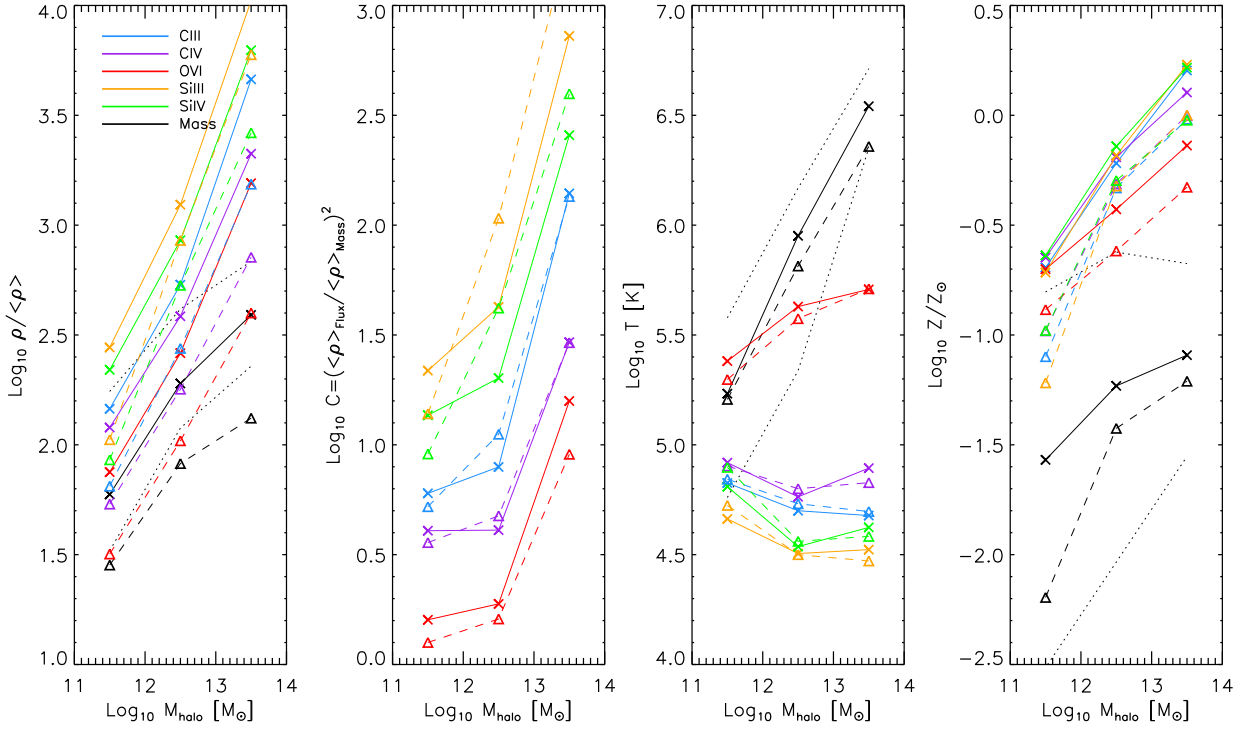

Figure 6.6: Mass-weighted (black curves) and UV flux-weighted (colours for different lines as in Figure 6.5 and indicated in the legend) median overdensity, clumping factor, temperature, and metallicity at $z = 0.125$ averaged over haloes with $M_{\rm halo} = 10^{11-12}$ $M_\odot$, 10^{12-13} $M_\odot$, and 10^{13-14} $M_\odot$, from left to right. The solid curves and crosses show the result for the gas at $0.1R_{\rm vir} - 0.5R_{\rm vir}$, while the dashed curves and triangles show $0.5R_{\rm vir} - R_{\rm vir}$. The dotted, black curves show the mass-weighted 16th and 84th percentiles for the inner halo.

The flux-weighted median metallicity is about an order of magnitude higher than the mass-weighted median metallicity and it is also higher than the mass-weighted 84th percentile. For high-mass haloes with $M_{\rm halo} > 10^{12}$ M$_\odot$, O VI probes gas with ~ 0.3 dex lower metallicities than the other lines. In the centres of groups the emission is dominated by gas with supersolar metallicities, even though on average the gas is enriched to $Z \approx 0.1$ Z$_\odot$. All computed metallicities increase with halo mass. Low-mass haloes with $M_{\rm halo} = 10^{11-12}$ M$_\odot$ have 0.6 dex lower mass-weighted metallicities in their outskirts as compared to their cores. This difference is somewhat smaller for flux-weighted metallicities and for higher mass haloes.

6.3.3 High-redshift UV

It is possible to detect rest-frame UV emitted at high redshift from the ground, in the optical. In the near future, several integral field unit spectrographs will become operational, such as the Multi-Unit Spectroscopic Explorer[5] (MUSE) on the *Very Large Telescope* (Bacon et al., 2010) and the Keck Cosmic Web Imager[6] (KCWI) on *Keck* (Martin et al., 2010). The Cosmic Web Imager[7] (CWI) is already installed on the 200-inch *Hale* telescope (Rahman et al., 2006; Matuszewski et al., 2010).

With narrow band observations it has already been demonstrated that diffuse Lyα emission can be detected down to $\sim 10^{-18}$ erg s^{-1}cm^{-2}arcsec^{-2} in individual objects (e.g. Steidel et al., 2000; Matsuda et al., 2004) and down to $\sim 10^{-19}$ erg s^{-1}cm^{-2}arcsec^{-2} in stacks (Steidel et al., 2011). New instrumentation, such as MUSE and KCWI[8], will allow us to go one order of magnitude deeper. This is essential for the detection of metal lines (Bertone & Schaye, 2012).

Figure 6.7 shows images of C III line emission at $z = 3$. We use halo mass bins of $M_{\rm halo} = 10^{10-11}$ M$_\odot$, 10^{11-12} M$_\odot$, and 10^{12-13} M$_\odot$ with $R_{\rm vir} \approx 0.06$, 0.14, and 0.29 h^{-1} comoving Mpc, respectively. The images are 0.5 h^{-1} comoving Mpc on a side, which corresponds to 22 arcsec on the sky at $z = 3$. The surface brightness is smoother than at $z = 0.125$ even though there are less haloes per bin, so the flux is coming from less clumpy material.

As before, we calculate the average of the surface brightness azimuthally for the metal-lines listed in Table 6.4. Figure 6.8 shows the mean (median) UV line surface brightness profiles at $z = 3$ as the solid (dotted) curves for the same three halo mass bins as in Figure 6.8. The surface brightness is about one order of magnitude lower at $z = 3$ than at $z = 0.125$ at a fixed fraction of $R_{\rm vir}$. Additionally, the profile shows a strong flattening inside 10 per cent of the virial radius. This is because we are probing down to smaller physical scales, where the emission is dominated by star-forming gas, which we have excluded from

[5]http://muse.univ-lyon1.fr/
[6]http://www.srl.caltech.edu/sal/keck-cosmic-web-imager.html
[7]http://http://www.srl.caltech.edu/sal/cosmic-web-imager.html
[8]http://www.srl.caltech.edu/sal/keck-cosmic-web-imager.html

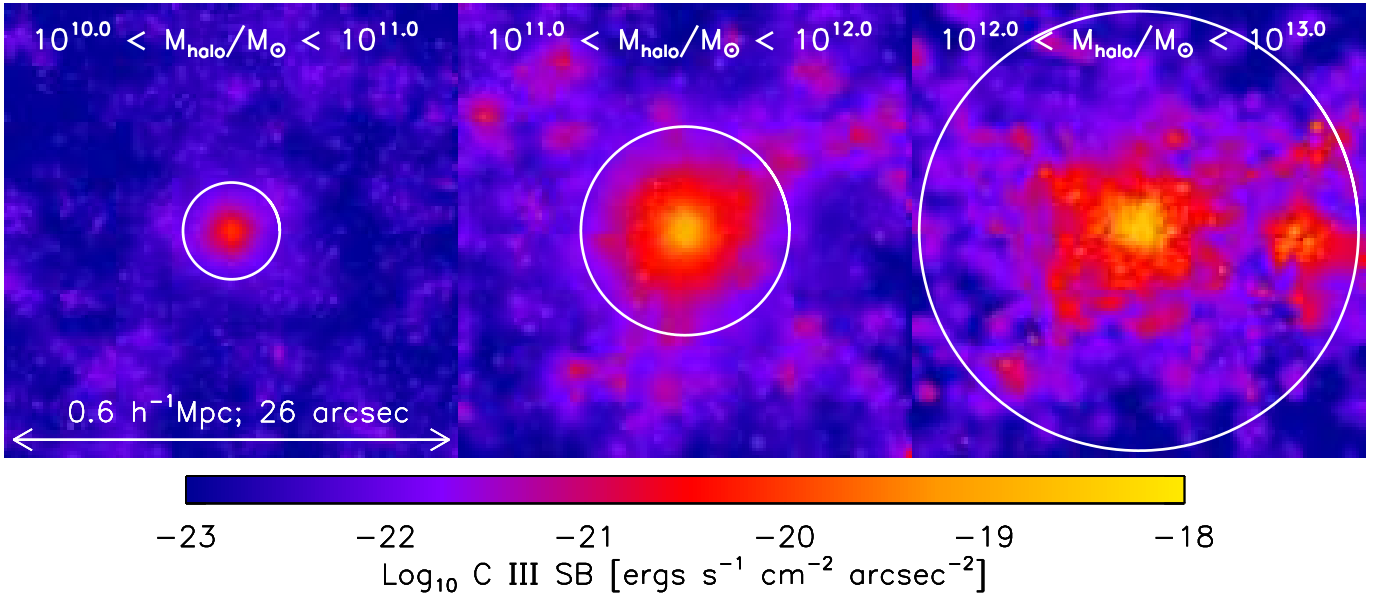

Figure 6.7: Mean CIII emission maps for haloes with $M_{\rm halo} = 10^{10-11}$ $M_\odot$, 10^{11-12} $M_\odot$, and 10^{12-13} $M_\odot$, from left to right, at $z = 3$. The images are 0.6 h^{-1} comoving Mpc on a side, span 26 arcsec on the sky, and have a pixel size of 0.2 arcsec. The white circles indicate the median virial radius.

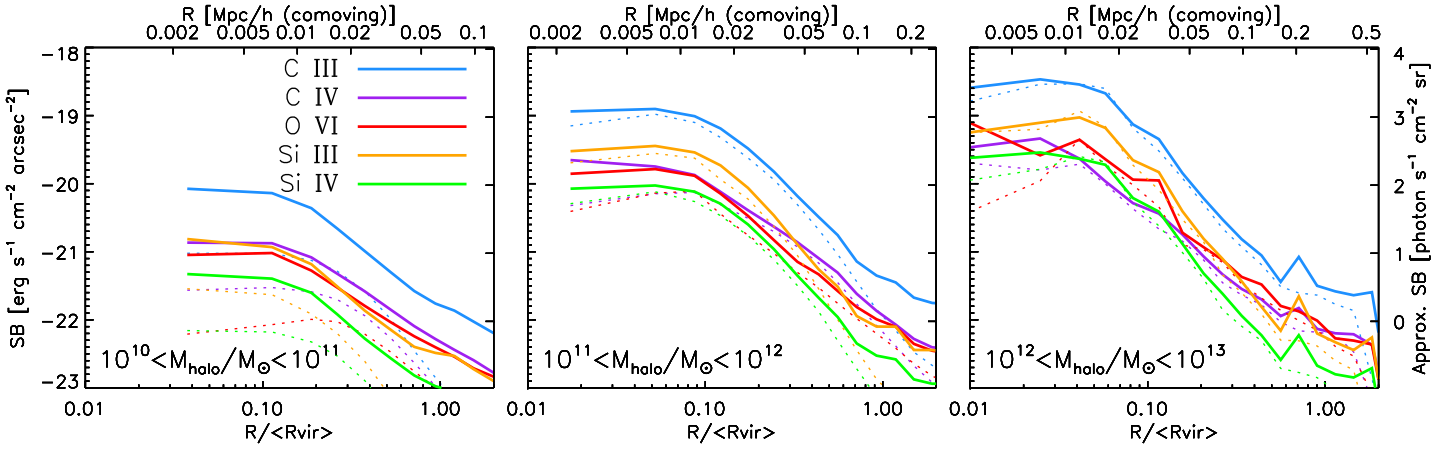

Figure 6.8: Mean UV surface brightness (solid curves) as a function of radius at $z = 3$ for the same haloes as in Figure 6.7. Dotted curves the median profile. The emission lines are indicated in the legend. The radius is normalized by dividing by the median virial radius in each mass bin. The surface brightness in erg $s^{-1}cm^{-2}arcsec^{-2}$ on the left y-axis is exact. For the right y-axis, it has been converted to photon $s^{-1}cm^{-2}sr^{-1}$ using $\langle\lambda\rangle = 1232$ Å. The pixel size was 0.2 arcsec before it was binned and the thickness of the region is 1.2 h^{-1} comoving Mpc. C III is the brightest line. C IV, Si III, and Si IV are of similar strength. The surface brightnesses are lower than at $z = 0.125$ and the flattening at small radii is more pronounced.

our calculations.

Comparing our metal-line results to the Lyα profile observed by Steidel et al. (2011) for $M_{\rm halo} \sim 10^{12}$ and $\langle z \rangle = 2.65$, we predict that the C III surface brightness is about 1–2 dex lower than the Lyα brightness. The other metal lines that are shown are about 0.5–1 dex fainter than C III. Because C III has a much shorter wavelength than Lyα, it is strongly absorbed by the intervening medium. It is therefore possible that the other metal lines are in fact stronger than C III. We calculated, but do not show, the Lyα surface brightness profile from our simulations in the optically thin limit and without a contribution from star formation. The observed profile is ~ 0.7 dex higher than the predicted profile, which is not surprising considering that the Lyα emission is thought to be originating from H II regions in the ISM.

With a detection limit of 10^{-20} erg s^{-1}cm^{-2}arcsec^{-2}, C III can be seen out to $0.3{\rm R_{vir}}$ for $M_{\rm halo} = 10^{11-12}$ M$_\odot$ and out to $0.2{\rm R_{vir}}$ for 10^{12-13} M$_\odot$ at $z = 3$. Other metal lines are weaker, but can still be probed to 10 per cent of $\rm R_{vir}$ for $M_{\rm halo} > 10^{11}$ M$_\odot$. Nothe, however, that the emission may in reality be brighter at these small radii, because we excluded emission from gas with $N_{\rm H} > 0.1$ cm^{-3}. We predict that the surface brightness for lower-mass haloes is below this limit.

In Figure 6.9 the UV flux-weighted overdensity, clumping factor, temperature, and metallicity are shown at $z = 3$ for the same metal lines as in Figure 6.6. The solid lines and crosses show the result for the gas at $0.1{\rm R_{vir}} - 0.5{\rm R_{vir}}$, while the dashed lines and triangles show $0.5{\rm R_{vir}} - {\rm R_{vir}}$. The general picture is unchanged at high redshift, although the density differences between different lines is somewhat reduced. The flux-weighted overdensities are lower, but the physical densities are higher at high redshift.

At $z = 3$ and for $M_{\rm halo} < 10^{12}$ M$_\odot$, O VI and C IV have clumping factors (see Equation 6.5) below unity, which means that the emission is biased towards lower-density regions. For the same haloes, $C \approx 1$ for C III emission and the clumping factor is 1–3 for the silicon lines. At higher halo masses, the clumping facor is $1 - 1.5$ dex higher and for most lines $C \approx 10 - 100$. Because the average temperature of the gas in these haloes is much higher than the temperature at which the emissivity of the UV metal lines peaks, the emission is originating from cold, dense clumps in the much hotter halo. For O VI the temperature difference and hence the clumping factor is smallest.

At $z = 3$ the scatter in density is larger than at $z = 0.125$: the difference between the 16th and 84th percentile is more than an order of magnitude as opposed to 0.4 dex. As a result, none of the lines are dominated by overdensities above the 84th percentile at this redshift. O VI and C IV are tracing densities below the median mass-weighted density for low-mass haloes ($M_{\rm halo} < 10^{12}$ M$_\odot$). The flux-weighted densities increase with halo mass, even if the mass-weighted density does not. The median density in the outskirts is lower than in the centre, for both flux- and mass-weighted quantities, by up to ~ 0.6 dex.

The flux-weighted temperatures are insensitive to halo mass. They trace temperatures near or above the median mass-weighted temperature for low-mass

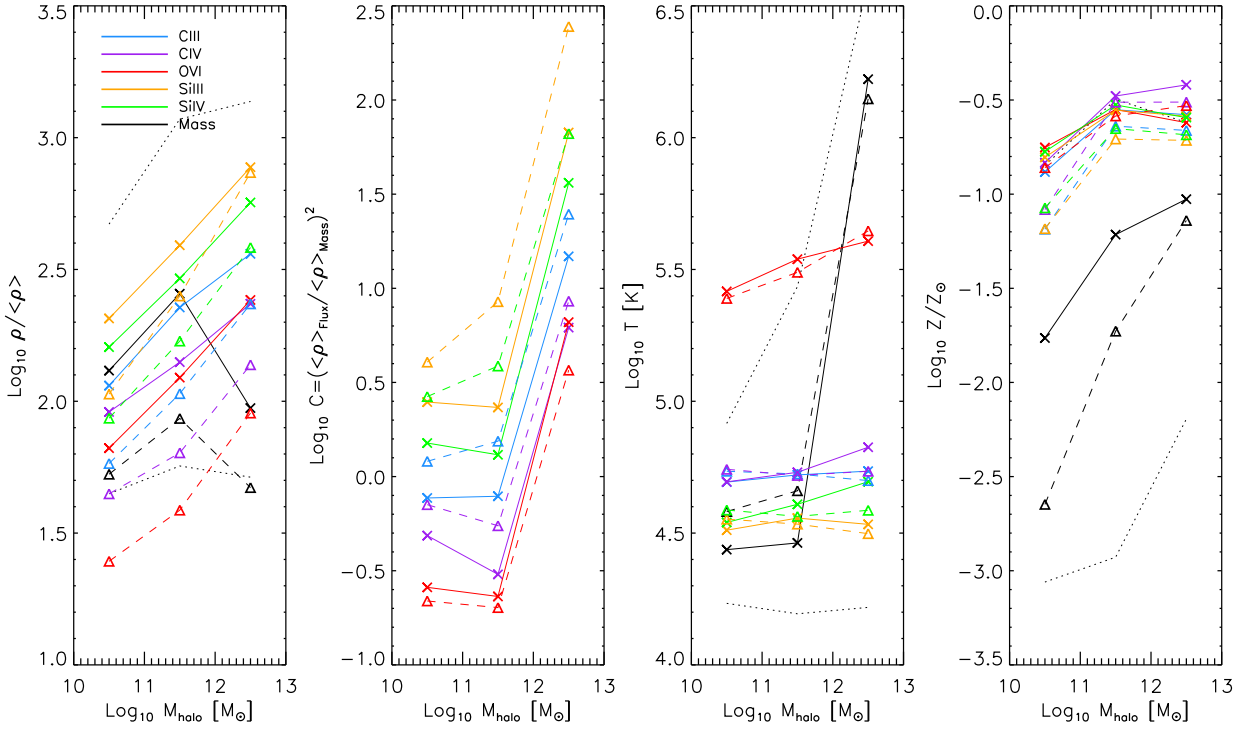

Figure 6.9: Mass-weighted (black curves) and UV flux-weighted (colours for different lines as in Figure 6.8 and indicated in the legend) median overdensity, clumping factor, temperature, and metallicity at $z = 3$ averaged over haloes with $M_{\rm halo} = 10^{10-11}$ $M_\odot$, $M_{\rm halo} = 10^{11-12}$ $M_\odot$, and $M_{\rm halo} = 10^{12-13}$ $M_\odot$, from left to right. The solid curves and crosses show the result for the gas at $0.1R_{\rm vir} - 0.5R_{\rm vir}$, while the dashed lines and triangles show $0.5R_{\rm vir} - R_{\rm vir}$. The dotted, black curves show the mass-weighted 16th and 84th percentiles for the inner halo.

haloes ($M_{\rm halo} < 10^{12}$ M$_\odot$), but the opposite is true for higher-mass haloes. The scatter in temperature increases with halo mass and becomes very large, with the mass-weighted 84th percentile 2.2 dex above the 16th percentile. This reflects the bimodal nature of halo gas in massive high-redshift galaxies, where the gas either has a temperature close to the virial temperature and or has $T < 10^5$ K (e.g. van de Voort & Schaye, 2012). O VI traces gas about an order of magnitude warmer than the other metal lines shown, because its emissivity peaks around $10^{5.5}$ K.

As we found before, the flux-weighted properties are biased towards high metallicities. All lines trace metallicities of about 0.1–0.4 Z$_\odot$ in the inner halo and $0.1 - 0.4$ dex lower in the outer halo. Because the spread in metallicity is much larger at $z = 3$ than at $z = 0.125$, the flux-weighted metallicities trace the mass-weighted 84th percentile at $z = 3$ as opposed to being significantly higher at $z = 0.125$.

6.3.4 Low-redshift Hα

Hα (6563 Å) emission at low redshift is observable with the same instruments as high redshift rest-frame UV emission. The predicted emission from gas around galaxies is shown in Figure 6.5 as a dashed, black curve. Interestingly, the Hα emission is comparable to C III emission at $R > 50$ kpc for all haloes with $M_{\rm halo} = 10^{11-14}$ M$_\odot$. However, for $R < 50$ kpc, Hα is much brighter than C III for the lowest halo mass bin ($M_{\rm halo} = 10^{11-12}$ M$_\odot$) and up to an order of magnitude fainter for the highest halo mass bin ($M_{\rm halo} = 10^{13-14}$ M$_\odot$). We stress again that we ignored emission from gas with $n_{\rm H} > 0.1$ cm^{-3}.

Assuming a limiting surface brightness of 10^{-20} erg s^{-1}cm^{-2}arcsec^{-2}, Hα emission from halo gas can be detected out to $0.5R_{\rm vir}$ for haloes with $M_{\rm halo} = 10^{11-12}$ M$_\odot$, $0.25R_{\rm vir}$ for haloes with $M_{\rm halo} = 10^{12-13}$ M$_\odot$, and out to $0.4R_{\rm vir}$ for group-sized haloes. This is feasible when stacking deep observations with MUSE or KCWI centred on galaxies.

6.4 Discussion and conclusions

A large fraction of the gas in galaxy haloes, groups, and clusters has temperatures $T = 10^{4.5-7}$ K (van de Voort & Schaye, 2012). At these temperatures, the cooling is dominated by metal-line emission for metallicities $Z \gtrsim 0.1$ Z$_\odot$ (e.g. Wiersma et al., 2009a). Observing these lines therefore constitutes an excellent route to studying the diffuse, warm-hot gas around galaxies, both at low and at high redshift. Additionally, metal-line emission may also provide us with clues as to how the circumgalactic gas was enriched and thus about the feedback process responsible for this enrichment.

We used cosmological, hydrodynamical simulations to quantify the surface brightness profiles of diffuse, circumgalactic gas, for both soft X-ray and rest-

frame UV metal lines. The lines we considered are C VI (0.367 keV), N VII (0.500 keV), OVII (0.561 keV), O VIII (0.654 keV), and Ne X (1.021 keV) in the X-ray band and C III (977 Å), C IV (1548 Å), Si III (1207 Å), Si IV (1294 Å), and O VI (1032 Å) in the rest-frame UV band. We discussed their detectability with current and future instruments and computed the flux-weighted physical properties of the gas in the halo core and outskirts.

The strongest soft X-ray line at redshift $z = 0.125$ is O VIII. It traces gas that is denser than the mass-weighted density, but the clumping factor is only a few for haloes with $M_{\rm halo} < 10^{14}$ M)$\odot$ and of order 10 for clusters. The temperature probed is within a factor of three from $10^{6.5}$ K, the temperature at which the emissivity peaks. It increases with halo mass, but less steeply than the mass-weighted temperature. The emission originates from regions with metallicities of about 0.3 $Z_\odot$, whereas the mass-weighted metallitcity is a factor of three lower. The difference between the inner and outer halo is largest for the flux-weighted density, about a factor of three. The other X-ray lines are biased towards the same densities, temperatures, and metallicity, but are at least a factor of three weaker.

The strongest UV metal-line, both at $z = 0.125$ and $z = 3$, is C III. The temperature of the gas the emission originates from is very close to $10^{4.7}$ K, the temperature at which the emissivity peaks, and does not vary with halo mass. At low redshift, the line is severely biased towards high metallicities. The flux-weighted metallicity is about an order of magnitude higher than the mass-weighted metallicity. At high redshift, the bias is smaller and the difference is a factor of a few. The clumping factor varies with halo mass from 10 to 100 at $z = 0.125$ and from 1 to 10 at $z = 3$. The flux-weighted overdensity increases from O VI to C IV to C III to Si IV to Si III by a facor of $\sim 3 - 10$. The Si III clumping factor reaches 10^3 in massive haloes. The temperature of the gas probed is about the same for all lines, except for O VI, whose emissivity peaks around $10^{5.5}$ K.

Proposed X-ray missions with detection limits of 10^{-1} photon $s^{-1}\,cm^{-2}\,sr^{-1}$ will be able to easily detect metal-line emission in galaxy haloes, groups, and clusters at $z = 0.125$. O VIII emission can be detected out to 80 per cent of the virial radius of groups and clusters and out to $0.4R_{\rm vir}$ for $M_{\rm halo} = 10^{12-13}$ $M_\odot$. C VI, N VII, O VII, and Ne X can also be detected out to smaller radii, $0.1 - 0.5R_{\rm vir}$.

Assuming a detection threshold of 10^{-20} erg s^{-1} cm^{-2} $arcsec^{-2}$, future optical instruments should be able to detect several rest-frame UV metal lines, C IV, O VI, Si III, and Si IV, out to $0.1R_{\rm vir}$ at $z = 3$ for haloes more massive than 10^{11} $M_\odot$. C III can be observed out to twice that distance. The same instruments can also observe Hα at low redshift, which provides a good probe of the cold (10^4 K) halo gas. Assuming the same detection threshold, Hα can be detected out to 0.2, 0.3, and 0.5 $R_{\rm vir}$ for $M_{\rm halo} = 10^{11-12}$, 10^{12-13}, and 10^{13-14} $M_\odot$, respectively. Because C III has a frequency blueward of Lyα, it may be strongly absorbed, especially when it is emitted at high redshift. The other UV metal lines may therefore be stronger.

If we assume the same detection limit of 10^{-20} erg s^{-1} cm^{-2} arcsec^{-2} for UV metal lines at $z = 0.125$, C III can be detected out to $0.3R_{\rm vir}$ for 10^{11-13} M$_\odot$ haloes and out to $0.5R_{\rm vir}$ for 10^{13-14} M$_\odot$ haloes. C IV, O VI, Si III, and Si IV can be detected out to $0.1 - 0.2$ R$_{\rm vir}$ for all haloes, and Si III can even be seen out to the same radius as C III for 10^{13-14} M$_\odot$ haloes.

Galaxies form inside (intersections of) filaments and we therefore expect that neighbouring galaxies are connected by these filaments. Stacking haloes randomly will not show filamentary emission, because the filaments will be oriented randomly. However, before stacking the galaxies, we can first rotate them towards their nearest neighbour of similar mass. This should enhance the emission of the gas in one direction. The signal at large radii is hard to detect, so the brightest emission lines should be chosen for this. We tested this using our simulations, but found that the enhancement is only about 0.2 dex (not shown).

Apart from stacking all images, one can stack only pixels with a detection in the brightest emission line and then look for emission from other lines. Because the emission is highest in the densest regions, the emission from different lines will be correlated. This also leads to an enhancement of the signal. Using pixels with a detection in Lyα would be well suited for detecting C III, C IV, Si III, and Si IV as these probe cold ($10^{4.5}$ K) gas.

In the near future, before we submit this paper to a journal, we will recompute the surface brightness profiles for simulations that include AGN feedback, because this feedback has been shown to be important (e.g. McCarthy et al., 2010; Bertone et al., 2010a). Additionally, we will test the dependence of our results on the resolution, pixel size, bin size of the surface brightness profile, and on the thickness of the region for which the emission is added.

Acknowledgements

We would like to thank Serena Bertone for allowing us to use the emissivity tables and all the members of the OWLS team for valuable discussions. The simulations presented here were run on Stella, the LOFAR BlueGene/L system in Groningen, on the Cosmology Machine at the Institute for Computational Cosmology in Durham as part of the Virgo Consortium research programme, and on Darwin in Cambridge. This work was sponsored by the National Computing Facilities Foundation (NCF) for the use of supercomputer facilities, with financial support from the Netherlands Organization for Scientific Research (NWO), also through a VIDI grant, and from the Marie Curie Initial Training Network CosmoComp (PITN-GA-2009-238356).